N. E. Schultz, A. W. Jasper, D. Bhatt, J. I. Siepmann, and D. G. Truhlar, in *Multiscale Simulation Methods for Nanomaterials*, edited by R. B. Ross and S. Mohanty (Wiley, Hoboken, 2008), pp. 169-188.

10

ALUMINUM NANOPARTICLES: ACCURATE POTENTIAL ENERGY FUNCTIONS AND PHYSICAL PROPERTIES

NATHAN E. SCHULTZ, AHREN W. JASPER, DIVESH BHATT, J. ILJA SIEPMANN, AND DONALD G. TRUHLAR

Department of Chemistry and Supercomputing Institute, University of Minnesota, Minneapolis, Minnesota

Aluminum, which has a very negative enthalpy of combustion, is a widely used ingredient in solid rocket propellants. Conventional formulations of solid rocket fuel use micrometer-sized aluminum particles; however, a number of studies have shown that the incorporation of nanometer-sized aluminum particles can greatly increase the energetic properties of the fuel.[1-4] There are two main ways in which nanoparticle formulations are beneficial for propellants and other energetic materials: (1) Smaller particles have a higher extent of conversion, which means that a higher percentage of fuel can be oxidized under practical combustion conditions as the particles decrease in size; (2) the burn rate increases greatly as the particles decrease in size.

The issues noted above and the fundamental need to understand the properties of nanoparticles have motivated the study of Al nanoparticles. One of the key goals in nanoparticle modeling is the ability to model particle properties as a function of size. A classic example of a size-dependent property is the melting point.[5,6] A number of studies have been carried out on the size-dependent melting points of Al clusters and nanoparticles,[7-9] and all indicate a melting-point that increases with particle size. The melting-point depression of small particles is important in understanding the physical characteristics of nanoparticles,

Multiscale Simulation Methods for Nanomaterials, Edited by Richard B. Ross and Sanat Mohanty

and it also has technological implications, affecting, for example, the igni temperature. Micrometer-sized Al particles are typically coated by a thick o> layer, which cracks during combustion because the pure Al interior of the part melts and significantly increases the internal pressure.[2] It is therefore poss that an earlier phase change during the heating process accompanying comb tion affects the ignition temperature, but quantitative estimates of the effect uncertain because the burn mechanism for nano-Al may be different from t for micrometer-sized Al particles. Nanoparticle simulations can provide use information about this mechanism and about other aspects of technologic important systems composed of metal nanoparticles.

In typical materials simulations, the Born–Oppenheimer separation of nucl and electronic motions[10] is assumed, and nuclear motion is governed by a sin ground-electronic-state potential energy function. This assumption is tenuous systems involving bulk metals, and one suspects that it is only approximat valid for metal nanoparticles as well. For small clusters, we may compute el tronic energy gaps accurately. For example, the first excited electronic state Al_2, $^3\Sigma_g^-$, is only 0.03 eV higher in energy than the ground state, $^3\Pi_u$,[11] and t first excited electronic state of Al_3, $^2A''_2$, is only 0.23 eV higher in energy th the ground electronic state, $^2A'_2$.[11] The size dependence of the highest occupi molecular orbital/lowest unoccupied molecular orbital gap for larger Al clu ters and nanoparticles is uncertain, but it is reasonable to expect that low-lyi electronic states may be involved in controlling the size dependence of certa properties of nanoparticles, such as enhanced reactivities. We note that nonadi batic effects have been observed in the reactions of Al atoms with hydrogen. Nevertheless, the Born–Oppenheimer ground-electronic-state potential ener surface is a practical starting point for simulations involving Al particles a their reactions with hydrogen or other heteroatoms.

When we assume that the Born–Oppenheimer approximation is valid, the in tial step in any simulation is the development and validation of a potential ener function. Reliable electronic structure calculations are quite affordable for sy tems with up to $\sim 10^2$ electrons[13], but the computations become less and le reliable as the particle size increases, due to the approximations that must b made. Therefore, it is common[14,15] in nanoparticle simulation to use comput tionally inexpensive, atomistic, analytic potential energy functions parameterize to reproduce experimental or computed bulk properties. One of the most impo tant characteristics of nanoparticle systems, however, is the dependence of the physical properties on particle size. Therefore, one of the key goals of nanoparti cle simulations is to model and predict trends in this size dependence, but usin potentials fit to bulk properties may introduce systematic size-dependent errors

The approach that we have taken in our nanoparticle work is to adjust analyti potential energy functions to fit electronic structure calculations for small A molecules, Al clusters, Al nanoparticles, and various bulk crystal phases as wel as experimental data for diatomic molecules and the observable bulk crysta phase. The primary property that we use for fitting is the geometry-dependen atomization energy (both absolute and relative), and we include a large numbe

of geometries both near and far from local minima. By doing this we implicitly include equilibrium bond lengths and forces. For Al, prior to our work, accurate data were unavailable for particles larger than a few atoms. The development of an Al database to fill this void is discussed in Section 1. We then discuss analytic potential energy functions and provide an example involving the size-dependent cohesive energy of Al in Section 2. In Section 3 we discuss in detail some recent simulations on the size-dependent properties of Al nanodroplets.

The phrase *particle size* is used to refer to the diameter or volume of a particle with a fixed number of atoms. (The phrase can also refer to the number of atoms in a particle.) There are many ways to compute the diameter of a particle. The approach that we take here is to compute the diameter d_{max} as the maximum Al–Al distance plus twice the van der Waals radius of Al, denoted r_{vdW}. For Al, r_{vdW} is 2.436 Å (discussed in Section 3). We can use this simple method to calculate how particle size depends on the number of Al atoms. We consider roughly spherical clusters and nanoparticles in which the atomic positions correspond to face-centered-cubic lattice sites. (The lattice constant used is 4.022 Å.[16]) The diameters for Al_n, with $n = 13$, 19, 55, 177, and 381, are then 1.04, 1.27, 1.61, 2.18, and 2.74 nm, respectively. To make a distinction between nanoparticles and clusters, we arbitrarily consider systems with fewer than 20 atoms to be clusters and those with 20 or more atoms to be nanoparticles.

1. NANO-AL DATABASE AND EFFECTIVE CORE SCHEME

The first step in developing the nano-Al database was to identify an affordable level of electronic structure theory that would provide accurate results for a wide range of clusters. There are two general classes of electronic structure theory: wave function theory[17,18] (WFT) and density functional theory[19,20] (DFT). State-of-the-art WFT methods are generally accurate to better than 0.04 eV per bond (1 kcal/mol per bond) for bond energies, and the most accurate WFT methods are accurate enough that they probably do not need to be specifically verified for Al clusters. The computational cost of these methods limits the feasibility of reliable ab initio WFT methods to approximately 10 Al atoms. DFT offers a more computationally affordable approach to calculating atomization energies, but due to the empirical nature of the best density functionals, the DFT methods themselves usually have to be specifically validated.

The first phase of the analytic potential energy function development was to determine how accurately DFT methods can treat small Al clusters. We used multicoefficient Gaussian-3/version 3[21] (MCG3/3) computations to develop[22] a small database of accurate bond energies for Al_n ($n = 2$ to 7). The MCG3/3 method[21] is a WFT method that is accurate to within 0.02 eV/atom when tested against the Database/3[21] collection of main group atomization energies. Using this database, we were able to assess the error of several DFT methods and identify the PBE0 functional[23,24] as a promising functional with an accuracy of 0.01 eV/atom when tested against the database of MCG3/3 calculated Al_n

atomization energies.[22] Because the general accuracy of MCG3/3 is 0.02 eV/atom, we can assign an error of 0.02 eV/atom to PBE0.

The PBE0 functional was assessed using the modified G3Large (MG3) basis set,[25,26] which is an all-electron basis set. [The MG3 basis set is equivalent for Al to the 6-311+G(3 d2f)[27–31] basis set.] The computational time required for a DFT calculation with the MG3 basis set becomes intractable as the size of the system grows, and the largest system we addressed at this level is Al_{13}, which is a 1.0-nm particle. This system requires 110 hours of computer time for a single-point energy calculation on a single processor of a Hewlett-Packard (HP) Itanium-2 computer. The affordability of these calculations can be increased greatly by replacing the all-electron basis set with a valence-electron basis set and replacing the core electrons by an effective core potential (ECP).[32] The combination of valence-electron basis set and ECP that we have developed (specifically for use with DFT methods) is labeled MEC (Minnesota effective core potential).[33] When tested against PBE0/MG3 calculations, the accuracy of the PBE0/MEC method is 0.01 eV/atom for atomization energies per atom (also called *cohesive energies*) and 0.005 Å for bond lengths. The database that we used for development of the analytic potential energy functions was created using the PBE0 functional with the MG3 basis set for systems with $n \leq 13$ and using the PBE0 functional with the MEC scheme for systems with $n = 14$ to 177. The computer time required for a single-point energy calculation with $n = 177$ is ~8000 hours (31 hours on 256 processors of a HP Itanium-2 computer).

We enforced the correct bulk limit on the analytic potential energy functions by including experimental values[16] for the cohesive energies, lattice constants, and bulk moduli of the face-centered-cubic (FCC) crystal phase. Accurate cohesive energies for the hexagonal-close-packed (HCP) and body-centered-cubic (BCC) crystal phases are included by adjusting calculated values[34] by a procedure that is described elsewhere.[35] Details of the database are also given elsewhere.[22,35] Some additional information about the database is provided in Section 3. We note briefly that we have included multiple points on the potential energy surface for each size cluster. By doing this, we fit to regions of the potential energy surface that would be visited during a finite-temperature simulation.

2. ANALYTIC POTENTIAL ENERGY FUNCTIONS

In previous work we tested and developed several analytic potential energy functions for Al. Here we present results for six analytic potential energy functions, and additional results can be found elsewhere.[35,36] We note that new and accurate potential energy functions[37] are being developed for condensed phase Al, but we do not survey those methods exhaustively.

The embedded atom model[38] has been widely used to study metal systems. For the embedded atom model, the potential energy, E, of the system is written as

$$E = \sum_{i>j} U_2(r_{ij}) + \sum_i F_i(\rho_i) \tag{1}$$

where r_{ij} is the distance between atomic centers i and j, U_2 is a pairwise interaction between atoms i and j, and F_i is a functional of the local electron density at the nucleus of atom i due to the other atoms; this density is called ρ_i. In many embedded-atom models, the embedding functional F is the square root of ρ_i, and ρ_i is approximated as a sum of pairwise additive terms. Note that the overall potential is not pairwise additive because F is nonlinear; nevertheless, U_2 and ρ_i are functions of single-pair distances, so the cost for evaluating the potential is just as manageable as that for a pairwise additive potential.

Several embedded-atom models that differ in their prescriptions for F_i, U_2, and ρ_i have been proposed[35,38–44] for Al. In this chapter we discuss five embedded-atom models: Ercolessi–Adams,[41] Mei–Davenport,[42,43] Sutton–Chen,[39] Streitz–Mintmire,[44] and NP-B.[35] The Mei–Davenport and NP-B models were chosen for detailed study here because in previous work[35] we reoptimized seven embedded-atom models against our database and found that the reparameterized Mei–Davenport model (which, as just explained, is called NP-B) gave the most accurate results. We also consider the Sutton–Chen, Streitz–Mintmire, and Ercolessi–Adams potentials because they have been used previously to simulate Al nanoparticles.[9,45–51]

The mean unsigned error per atom for NP-B is 0.05 eV/atom, whereas the Mei–Davenport fit has a mean unsigned error per atom of 0.18 eV/atom. This improvement in accuracy shows that the physical form of the Mei–Davenport potential energy function is flexible enough to describe the bonding of Al atoms in different bonding situations, but that the data used to obtain the original parameters (which included only bulk data) were not diverse enough to provide an accurate potential energy function for Al clusters and nanoparticles. This comparison shows that it is important to have a robust data set in addition to having an appropriate physical form for the potential energy function.

We also consider the NP-A analytic potential energy function,[35] which was also developed using the Al database discussed above. This function has the form

$$E = \sum_{i>j} V_2(r_{ij}) f_{ij}^{\mathrm{MB}} \tag{2}$$

where V_2 is the two-body interaction fitted to the extended-Rydberg[52,53] functional form, and f_{ij}^{MB} is a many-body function that deviates from unity when atoms i and j interact with other atoms. Several prescriptions for f_{ij}^{MB} were tested[35] using the database discussed above, and an accurate fit was obtained with $f_{ij}^{\mathrm{MB}} = f_{ij}^{\mathrm{S}} f_{ij}^{\mathrm{CN}}$, where f_{ij}^{S} is a screening function that weakens the bond between atoms i and j if other atoms are in between atoms i and j, and f_{ij}^{CN} incorporates the dependence of the bond order on the coordination numbers of the participating atoms.

To illustrate the screening term, we consider a system of three Al atoms (see Figure 1). In the figure the coordinates of atoms 1 and 2 are held fixed and atom 3 moves along coordinate R. Physically speaking, the interaction between atoms 1 and 2 is screened by the presence of atom 3 as atom 3 moves along a R. The

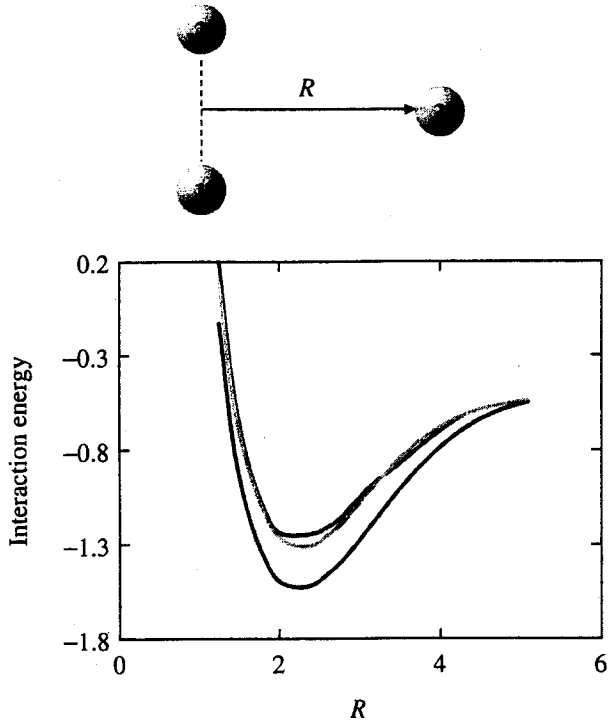

Figure 1 In this model system, atoms 1 and 2 are held fixed and atom 3 moves along coordinate R (Å). Atoms 1 and 2 are separated by 2.8635 Å. The interaction energy (in eV/atom) for this system is plotted with a well depth of <1.3 for PBE0/MG3, with a well depth of 1.55 for an accurate two-body interatomic potential [Eq. (3)], and with a well depth of ~1.3 for a two-body interatomic potential that is modified by a screening term [Eq. (4)] with parameters of the ER2+ES potential.

interaction energy is plotted in Figure 1 as a function of R for the following two potentials:

$$E = \sum_{i>j} V_2(r_{ij}) \tag{3}$$

and

$$E = \sum_{i>j} V_2(r_{ij}) f_{ij}^{S} \tag{4}$$

where Eq. (3) is simply the two-body interaction without many-body effects and Eq. (4) is the two-body interaction modified only by the screening term. [In previous work,[36] Eq. (4) was denoted ER2 + ES.] We can see from Figure 1 that the two-body interaction alones significantly overestimates the three-body interaction energy and the screening function allows for a more accurate description of the three-body interaction. In addition to predicting a more accurate binding energy for Al_3, Eq. (4) also predicts a more physical repulsive wall.

In addition to screening, which is a three-body effect, we also consider the effect of coordination number, which in bulk Al is 12. We note that screening and coordination number effects are related; that is, the presence of the third atom in Figure 1 raises the coordination number of atoms 1 and 2, and a highly

coordinated atom involves pairs of atoms being screened by nearby atoms. However, we found it useful to treat these effects separately and to include coordination number effects explicitly. To illustrate the effectiveness of the coordination number term, we consider a potential energy function of the form

$$E = \sum_{i>j} V_2(r_{ij}) f_{ij}^{\mathrm{CN}} \tag{5}$$

In previous work,[36] Eq. (5) was denoted ER2 + ECN. The cohesive energy of the ground state of icosahedral Al_{13} (which consists of a central atom coordinated to 12 atoms and 12 surface atoms each coordinated to six atoms) computed with PBE0/MEC is 2.5 eV/atom. The cohesive energies of the same structure computed with Eqs. (3) and (5) are 5.5 and 2.5 eV/atom, respectively. The pairwise additive potential energy function in Eq. (3) overestimates the interaction energy of Al_{13} by 3 eV/atom, and the coordination number factor corrects this error.

As mentioned above, the screening and coordination number factors are related, and in fact Eqs. (4) and (5) have similar overall errors when tested against the full database. However, the cohesive energy of Al_{13} computed with Eq. (4) is 3.4 eV/atom and is less accurate than Eq. (5) for this property. We find in general that the effect of including the coordination number term is more significant for bigger clusters (which have the largest contribution to their total energies from coordination effects), whereas the reduction in the error due to the incorporation of the screening term is more evenly distributed.

Physically, one expects that there is some cutoff distance at which the interaction between two atoms may be set to zero. We have therefore built cutoffs into the functional forms of NP-A and NP-B. When using a cutoff distance, the cost to evaluate the analytic potential energy function scales as n in the large-n limit. Such linear scaling is achieved for the NP-A potential by multiplying the terms in Eq. (2) by a cutoff function,[54] which goes smoothly to zero at $r_{ij} = 6.5$ Å. Without a cutoff, the computational cost of the screening and coordination number factors both scale as n^3. The range parameter of the cutoff function was optimized during the fitting procedure to avoid numerical and convergence problems that can arise when applying cutoffs during simulations. The cutoff function for the NP-B analytic potential energy function goes to zero at 5.38 Å. Without the cutoff function, the computational cost of evaluating the embedding term scales as n^2, where n is the number of atoms in the system. Both potentials (NP-A and NP-B) begin to scale linearly at ~10,000 atoms. However, the cutoff functions give significant cost reductions for smaller clusters. For example, the average CPU cost of an energy evaluation of Al_{1055} with NP-A and NP-B on an IBM Power4 computer is reduced by factors 5 and 2, respectively.

In Figure 2 we plot the mean unsigned error[35] (in eV/atom) for the five potentials for groups of various particle sizes. The groups contain particle sizes with $n = 2$, 3, 4, 7, 9 to 13, 14 to 19, 20 to 43, 50 to 55, 56 to 79, 80 to 87, and 89 to 177, respectively, and are labeled by the average number of atoms in the particles of that bin, which are 2, 3, 4, 7, 13, 18, 33, 53, 71, 86, and 124, respectively.

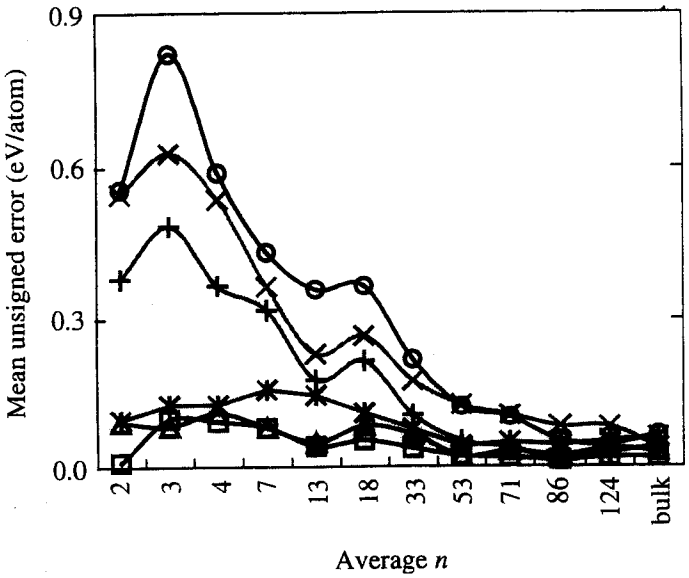

Figure 2 Mean unsigned error (in eV/atom) grouped by particle size for the Ercolessi–Adams (*), Mei–Davenport (×), NP-A (□), NP-B (Δ), Streitz–Mintmire (+), and Sutton–Chen (○) potential energy functions of the average particle size in a bin.

The most accurate potential for clusters ($n = 2$ to 20), nanoparticles (21 to 177), and the bulk crystal phase is NP-A. The Mei–Davenport, Streitz–Mintmire, and Sutton–Chen PEFs were not fit to nanoparticle or cluster data and have a more size-dependent error. On the one hand, it might be argued that it is unfair to test the bulk- fitted potentials against nanoparticles and clusters, but on the other hand, it can be argued that these studies are very important because these potentials are sometimes used in nanoparticle simulations without validation.[9,45–49]

The Ercolessi and Adams analytic potential energy function[41] was fit (by the original authors[41]) to Al cluster and surface data and to bulk crystal data. The mean unsigned error (MUE) per atom for this analytic potential energy function (when evaluated with our database) is less dependent on the number of atoms than the error for the Mei–Davenport, Streitz–Mintmire, and Sutton–Chen analytic potential energy functions; however, it has a larger mean unsigned error (MUE) per atom than either the NP-A or NP-B PEF. The total MUE for the Ercolessi and Adams analytic potential energy function is 0.11 eV/atom, whereas the NP-A and NP-B analytic potential energy functions have MUE values of 0.03 and 0.05 eV/atom, respectively. The fitting data used by Ercolessi–Adams was obtained (by the original authors) from the local density approximation to DFT,[55,56] which is not usually quantitatively accurate for metals,[57] whereas our data was obtained from a validated[22] hybrid DFT method (PBE0). The improved accuracy of our analytic potential energy functions is due, then, to the quality of fitting data, which again highlights the need to have not only physical functional forms but also accurate fitting data.

An interesting example of how the errors depend on the number of atoms is to look at the cohesive energies of nanocrystals, which are nanometer-sized objects with a structure cut from a bulk crystal. In this chapter we discuss FCC

nanocrystals, which are nanoparticles that have the same local arrangement of atoms that is found in FCC crystals. An FCC crystal is generated around a central atom using a lattice parameter. The distance from the central atom in an FCC cluster to another atom i in the cluster is denoted R_i, and due to the periodic nature of the crystal, there is a unique set, S_m, of values for R_i, where m is an index. Nanocrystal m is defined as a nanocrystal containing all of the atoms with $R_i < S_m$. For an FCC crystal, the nanocrystals studied here have $n = 13$, 19, 43, 55, 79, 87, 135, and 177, where n is the number of Al atoms. Thus, this sequence of values defines a unique set of FCC nanocrystals that have geometric magic numbers. It also possible to define nonunique FCC nanocrystals for $n = 14$ to 18 and 20 to 42, which are also studied in this chapter. The strategy that we employ for determining the coordinates of these nonunique nanocrystals is based on our determination of the lowest-energy geometry. For Al_{14}, an atom is placed at one of the available and equivalent FCC lattice sites between nanocrystal Al_{13} and Al_{19}. There are now four nonequivalent unoccupied lattice sites in which an atom can be located to form Al_{15}, and the energy with each of these lattice sites occupied is evaluated with PBE0/MEC to determine which isomer of Al_{15} is the lowest in energy. The same procedure is followed for $n = 16$ to 18 and $n = 20$ to 42.

In Figure 3 we plot the cohesive energies computed with the PBE0/MEC DFT method and by the MeiD, NP-A, NP-B, StrM, and SutC analytic potential energy functions for FCC nanocrystals with $n = 13$ to 43, 55, 79, 87, 135, and 177. The lattice constant is optimized for each nanocrystal with the same method, PBE0/MEC or an analytic potential energy function, that is used to calculate the cohesive energy of that nanocrystal. For example, the cohesive energies calculated with NP-A also use lattice constants that are calculated with NP-A. The only potentials that are accurate across this entire size range are NP-A and NP-B, with NP-A being more accurate. The StrM potential is accurate for $n \gtrsim 20$ and is less accurate for $n \lesssim 20$. This behavior in the StrM potential can also be seen in Figure 2. The other two potentials, MeiD and SutC, have errors that are approximately 0.1 eV/atom for nanoparticles larger than $n = 55$, and the errors grow to 0.3 to 0.4 eV/atom for smaller nanocyrstals.

All of the analytic potential energy functions presented in this chapter break down to some extent for small n, where n is the number of atoms. NP-A is built on an accurate two-body interaction, so the dimer is quantitatively accurate for NP-A. The NP-B analytic potential energy function does reasonably well for the dimer (see Figure 2), but both NP-A and NP-B cannot predict the correct geometries for Al_4 or Al_5. Al_4 and Al_5 are known to be planar,[11,58,59] but the analytic potential energy functions predict Al_4 and Al_5 to be three-dimensional. It is possible to develop analytic potential energy functions to predict planar geometries for Al_4 or Al_5,[58] but these analytic potential energy functions are inaccurate for larger clusters. For example, the analytic potential energy function of Pettersson et al.[58] that predicts Al_4 and Al_5 to be planar also predicts Al_{13} to be planar and has a 0.7-eV/atom error for the bulk cohesive energy.[58] One way to understand this problem is by comparing the total coordination numbers of

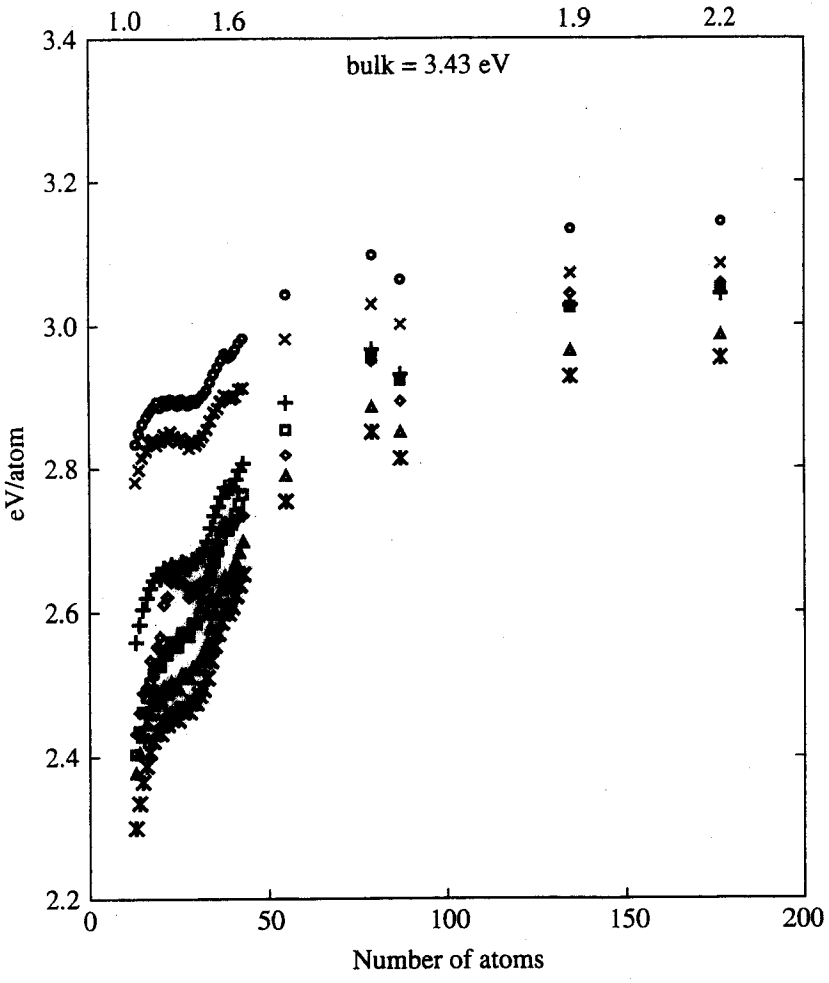

Figure 3 Cohesive energy (in eV/atom) for FCC nanocrystals computed with PBE0/MEC (◇) and the Ercolessi–Adams (⌈), Mei–Davenport (×), NP-A (□), NP-B (⌈), Streitz–Mintmire (+), and Sutton–Chen (○) potential energy functions as functions of the number of atoms (along the bottom) and particle diameter (along the top).

the Al atoms in planar and nonplanar clusters. The total coordination number is defined as the sum of coordination numbers for all of the atoms in a cluster. For example, Al_3 (equilateral triangle) has a total coordination number of 6 because each of the atoms is bonded to two other Al atoms. For Al_4, the planar structure (D_{2h} symmetry) has four atoms with a coordination number of 2 for a total coordination number of 8, whereas the nonplanar structure (T_d symmetry) has four atoms with a coordination number of 3, for a total coordination number of 12. Thus, a structure with a total coordination number of 8 is lower in energy than a structure with a total coordination number of 12. For Al_5, the planar structure (C_{2v} symmetry) has a total coordination number of 16, whereas the nonplanar structure (T_d symmetry) has a total coordination number of 20. However, the ground state of Al_6 is three-dimensional (O_h symmetry) and has a total coordination number of 24, and the lowest-energy planar structure of Al_6 (C_{2h} symmetry) has a total coordination number of 20. These considerations show why it is very difficult to develop many-body functional forms that fit all these clusters; such functions

must favor low coordination numbers for Al_4 and Al_5 but higher coordination numbers for Al_6 and larger. We have only examined structural isomers where the coordination number differs between isomers and not clusters, and that have the same coordination number but different structural isomers.[60]

3. NANOPARTICLE SIMULATIONS

Simulation Procedure

The potential used for the simulations is the NP-B embedded-atom model. The nanoparticles are simulated via Metropolis Monte Carlo[61] in a canonical ensemble where the number of atoms, box size, and temperature are fixed. Al_n nanoparticles with $n = 55$, 400, and 1000 were simulated with periodic boundary conditions with cubic box lengths of 35, 45, and 60 Å, respectively. For the 55-atom system, the starting structure is an energy (NP-B potential) minimized icosahedral nanoparticle. The starting structure for 400- and 1000-atom systems is a FCC nanocrystal. Accordingly, the size of the box in each case is larger enough that the periodic images of a nanoparticle do not interact. Consequently, the particles are treated essentially as isolated nanodroplets in each case.

Nanoparticle Diameters

There are many ways that one can compute the diameters of nanoparticles. We compute the particle diameters as the maximum distance between two atoms plus twice the van der Waals radius of Al. The van der Waals radius for Al is 2.346 Å (see below). The particles discussed in this section were optimized with the NP-B potential unless otherwise specified. The diameters for all the particles in this section are given in Table 1.

The first particle that we discuss is Al_{13}. Al_{13} is a special cluster because it is the first cluster that can have an atom with a coordination number of 12. An Al atom in a periodic FCC lattice also has a coordination number of 12; therefore, Al_{13} is the smallest cluster to have an interior "bulklike" atom and surface atoms. The global minimum[33] of Al_{13} (icosahedron) found with NP-B at 0 K has $d_{max} = 1.09$ nm. The FCC-nanocrystal for Al_{13} has $d_{max} = 1.02$ nm. The global minimum of Al_{19} with the NP-B potential (double-icosahedron) has $d_{max} = 1.26$ nm, and the FCC-nanocrystal has $d_{max} = 1.29$ nm. The ground-state structure of Al_{55} with the NP-B potential is icosahedral with $d_{max} = 1.55$ nm, whereas the FCC-nanocrystal has $d_{max} = 1.58$ nm. From these results we can see that the diameters of the particles for a given number of atoms are not very sensitive to the crystal structure, as the FCC-nanocrystals and icosahedral nanoparticles for a given number of atoms differ by an average of 0.04 nm. We conclude that the particle diameter is, to a first approximation, independent of crystal structure.

The structures for Al_{400} and Al_{1000} were optimized with the NP-B potential. The starting geometries were the globally optimized geometries for the

TABLE 1. Maximum Al–Al Distance d_{max} (nm) for Several Al Particles Computed Using the NP-B Embedded-Atom Model

Number of Atoms	Structure	D_{max}
	$T = 0$ K	
13	FCC-nanocrystal	1.09
	global minimum[a]	1.02
19	FCC-nanocrystal	1.26
	global minimum[a]	1.29
55	FCC-nanocrystal	1.58
	global minimum[a]	1.55
400	global minimum[b]	2.72
1000	global minimum[b]	3.77
	$T = 1000$ K	
55	ensemble average	1.71
400	ensemble average	3.00
1000	ensemble average	3.92
	$T = 1500$ K	
55	ensemble average	1.80
400	ensemble average	3.11
1000	ensemble average	4.10
	$T = 2000$ K	
55	ensemble average	1.88
400	ensemble average	3.24
1000	ensemble average	4.21
	$T = 2500$ K	
55	ensemble average	1.97
400	ensemble average	3.42
1000	ensemble average	4.38

[a]Icosahedral.
[b]The geometry was optimized by starting with the global minimum for a Lennard-Jones particle (see the text).

Lennard-Jones system,[62] where the initial coordinates were scaled by 3.00. The coordinates for the Lennard-Jones system were obtained from the Cambridge Cluster Database.[62,63] For optimized Al_{400} and Al_{1000}, $d_{max} = 2.72$ and 3.77 nm, respectively. It is reasonable to expect that the diameters would change by less 0.1 nm if a more exhaustive search for the global minimum were conducted.

The average d_{max} values for nanodroplets (Al_n with $n = 55$, 400, and 1000 with $T = 1000$ to 2500 K) are also given in Table 1. We note initially that for all droplet sizes d_{max} with $T \geq 1000$ K is greater than d_{max} with $T = 0$ K, which is an expected result. The interesting aspect of these d_{max} values is that the diameters increase at different rates, depending on the number of atoms in the droplet. To explore this, we have fit (d_{max},T) to a linear equation,

$$d_{max} = \beta T + b \tag{6}$$

where the slope of the line, β, indicates how rapidly d_{max} increases with T. The intercept, b, would in principle be the value of d_{max} at $T = 0$, but we do not expect d_{max} to remain linear with T as the particles undergo a phase change from liquid to solid. The values of β for Al_n with $n = 55$, 400, and 1000 are 3.0×10^{-3}, 2.8×10^{-3}, and 1.7×10^{-3} K^{-1}, respectively. We can see that β increases with an increasing number of atoms and that the response of d_{max} to T is a size-dependent property.

Density and Thermal Expansion

A fundamental property of any material is the density. The density is unambiguous for bulk materials, but for nanoparticles it requires a definition of the volume of the nanoparticle. Here, we calculate the nanoparticle volume by using the method of overlapping van der Waals spheres.[64] We denote the density computed from the number of particles and the volume of overlapping van der Waals spheres as ρ_{vdW}. In this method, the only input that is required is the van der Waals radius for Al. The van der Waals radius, r_{vdW}, that we use for Al is 2.346 Å. This value was obtained from the bond length of AlNe and Ne_2 by the relationship

$$r_{vdw}(Al) = r_e(AlNe) - \frac{1}{2} r_e(Ne_2) \tag{7}$$

where r_e(AlNe) and $r_e(Ne_2)$ are the bond lengths of AlNe and Ne_2, respectively. We computed r_e(AlNe) and $r_e(Ne_2)$ to be 3.894 and 3.099 Å, respectively, using WFT. The electron correlation method used was coupled cluster theory with single and double substitutions and quasiperturbative triples, CCSD(T),[65–67] and the one-electron basis set used was the aug-cc-pV5Z[68] basis set.

We can also compute the covalent radii, r_{cov}, of Al by first computing the bond length of Al_n particles that, by symmetry, have one unique Al–Al bond length. We have computed the bond length using the PBE0 density functional with the MEC scheme. The Al_n clusters that we examined are Al_2, Al_3 with D_{3h} symmetry, and Al_{13}, Al_{55}, and Al_{177} FCC-nanocrystals. The small clusters, Al_2 and Al_3, have $r_{cov} = 1.365$ and 1.253 Å, respectively. The FCC-nanocrystals have $r_{cov} = 1.923$, 1.938, and 1.985 Å, respectively. The zero-point-exclusive experimental lattice constant[16] at 0 K implies an equilibrium internuclear distance of nearest neighbors of 4.022 Å, which corresponds to $r_{cov} = 2.011$ Å.

As stated earlier, the densities are computed from overlapping van der Waals spheres, which use r_{vdW}. We have seen that r_{cov} can depend on the number of Al atoms. It is also likely that r_{vdW} depends on the number of atoms in the clusters. This is one unsatisfactory part of our method for computing volumes. An additional unsatisfactory aspect of this method for computing volumes is that voids are excluded from the total volume, and the total volume associated with voids may be nonneglible as the temperature is increased. The major drawback to excluding voids is that it does not allow a meaningful comparison to experiment or a bulk simulation. In a bulk simulation, the density of a liquid is computed from the number of atoms within the simulation box and volume of the box. In this manner, voids are included in the total volume of the liquid. In bulk experiments, the density of liquid aluminum is determined by melting a millimeter-sized piece of Al and measuring the diameter and mass of the drop.[69] In this manner, voids are once again included in the total volume. An alternative way[70] to obtaining the nanoparticle volumes would be to roll a probe sphere over the surface of the nanoparticle. This would eliminate the contribution of internal voids, but it will introduce parameter-dependent oscillations in the surface area.

In Table 2 we give the computed nanoparticle densities, ρ_{vdW}. We also include experimental values of the density of bulk liquid.[69] We denote the experimental value of the density of the bulk liquid as ρ_{exp}. We can see that the ρ_{vdW} values are always lower than the experimental values for the bulk liquid. This is not entirely unexpected, as the nanoparticle densities should be lower due to surface effects, but it is not clear what significance should be attached to this

TABLE 2. Coefficient of Thermal Expansion, α (10^{-5} K^{-1}) for Al_{55}, Al_{400}, and Al_{1000}; Density, ρ (g/mL); and the Sphericality Parameter, L (Unitless)

	ρ_{vdW}			Bulk Liquid	
Property	Al_{55}	Al_{400}	Al_{1000}	ρ_{bulk}[a]	ρ_{exp}[b]
V					
1000 K	1.67	1.96	2.06	2.30	2.36
1500 K	1.61	1.88	1.97	2.19	2.25
2000 K	1.55	1.81	1.89	2.09	2.13
2500 K	1.50	1.73	1.82	2.00	2.01
α	6.77	7.79	7.93	8.86[c]	9.91[d]
L					
1000 K	0.88	0.94	0.95		
1500 K	0.84	0.93	0.94		
2000 K	0.82	0.91	0.94		
2500 K	0.79	0.88	0.94		

[a]Calculated by extrapolating the nanodroplets volumes using $\rho_{vdW} = aN^{-1/3} + \rho_{bulk}$, where N is the number of atoms.
[b]Experimental density.
[c]Calculated from ρ_{bulk}.
[d]Calculated from ρ_{exp}.

finding because of the volume of nanoparticle voids. For example, if we fit the density of Al_{55}, Al_{400}, and Al_{1000} with $T = 1000$ K to $\rho_{vdW} = \alpha N^{-1/3} + \rho_{bulk}$, we find that $\rho_{bulk} = 2.30$ g/mL. The value of ρ_{bulk} corresponds to the bulk density, and it differs from the experimental value of 2.36 g/mL by 0.06 g/mL. The discrepancy between the calculated and expected values cannot be attributed only to the presence of voids because correcting for voids would increase the calculated density. We have also found that we can change the values of ρ_{bulk} and ρ_{vdW} by changing the value of r_{vdW}. For example, decreasing the van der Waals radius by 23% to 1.9 Å increases the density of Al_{1000} at 1000 K to 2.31 g/mL (+12%) and increases ρ_{bulk} at 1000 K by 2.41 g/mL (+5%). Due to the differences in ρ_{bulk} and ρ_{exp}, it might be more appropriate to compare ρ_{vdW} to ρ_{bulk} than to ρ_{exp}. Values of ρ_{bulk} and ρ_{exp} for all of the temperatures are given in Table 2.

By comparing the nanoparticle densities (ρ_{vdW}) to the extrapolated bulk densities (ρ_{bulk}), we can see that the nanodroplets expand with temperature at a different rate than does the bulk liquid. To quantify this, we calculate the coefficient of thermal expansion. For the nanodroplets the coefficient of thermal expansion, α_{vdW}, is calculated as

$$\alpha_{vdW} = \frac{1}{V}\frac{dV_{vdW}}{dT} \tag{8}$$

where V_{vdW} is the volume computed from overlapping van der Waals spheres. For the bulk liquid, we compute α_{bulk} as

$$\alpha_{bulk} = \rho_{bulk}\frac{d(1/\rho_{bulk})}{dT} \tag{9}$$

where ρ_{bulk} is defined in the preceding paragraph. We have computed ρ_{bulk} at $T = 1000$, 1500, 2000, and 2500 K and then fitted $(1/\rho_{ex}, T)$ to a linear line to obtain α_{bulk} for the bulk liquid. The computed values of α_{bulk} are given in Table 2 along with the experimental value, α_{exp}, for this quantity. We compute α_{exp} by replacing ρ_{bulk} with ρ_{exp} in Eq. (9).

We first talk about α_{bulk} and α_{exp}. The values of α_{bulk} and α_{exp} are 8.9×10^{-5} and 9.9×10^{-4} K^{-1}, respectively. The agreement between α_{bulk} and α_{exp} is very good, despite the approximations that are involved in calculating α_{bulk}. Turning now to the nanodroplets, we can see from Table 2 that α_{vdW} is a size-dependent property that decreases with decreasing particle size. For the smallest droplet, Al_{55}, the computed α_{vdW} is 6.8×10^{-5} K^{-1}, and that is 69% of α_{bulk}; however, for the largest particle, Al_{1000}, the computed α_{vdW} is 7.9×10^{-5} K^{-1}, 89% of α_{bulk}.

The size dependence of the coefficient of thermal expansion has previously been studied by Pathak and Shenoy for systems below the melting point.[51] The coefficient of thermal expansion that Pathak and Shenoy[51] calculated is denoted as α_{stress}, because it is computed from the temperature-dependent stress tensor, whereas we calculate α_{vdW} from volume changes. Also, α_{stress} is computed for nanometer-thick slabs with two-dimensional periodicity, and α_{vdW} is for liquid

droplets. The values of α_{stress} for 2.0-, 3.2-, and 4.0-nm-thick slabs are 4.6×10^{-5}, 5.3×10^{-5}, and 5.6×10^{-5} K^{-1}, respectively.

In this chapter we chose to focus on the similar behavior of α_{stress} and α_{vdW} rather than the differences between the two quantities. The results of Pathak and Shenoy[51] showed that α_{stress} increases with decreasing slab thickness for a Lennard-Jones system, whereas they showed that α_{stress} decreases with decreasing slab thickness for an Al system. (Pathak and Shenoy[51] modeled the Al slab with the embedded atom model of Ercolessi and Adams.[41]) Whether α_{stress} increases or decreases with decreasing particle size depends on the type of system being studied. The results of Pathak and Shenoy[51] agree qualitatively with our results, as we find that α_{vdW} decreases with decreasing system size.

Earlier we discussed the dependence of particle diameter, d_{max}, on T, where this relationship was quantified through β in Eq. (6). We saw that β increases with increasing particle size as α_{vdW} does. It is clear that these two quantities, β and α_{vdW}, are related, as they both pertain to changes in particle size with temperature.

Shapes

Another fundamental property of a nanoparticle is its shape. It is sometimes assumed,[4] due to lack of better information, that Al nanoparticles are spherical. We are able to quantify the shape of a nanodroplet by using the sphericality parameter, L, of Mingos et al., which is defined as

$$L = \frac{3I_{unique}}{\sum_{i=1}^{3} I_i} \tag{10}$$

where I_i is the principal moment of interia i and I_{unique} is the unique principal moment of inertia. I_{unique} is defined as the principal moment of interia that deviates most from the average principal moment of inertia. Using this definition, $L = 1$ for a sphere, $0 \leq L < 1$ for an prolate spheroid, and $1 < L \leq 1.5$ for an oblate spheroid. The sphericality parameter for a cylinder that has the length and width of a football is 0.51, whereas L for a hockey puck is 1.40.

The sphericality parameters for the nanodroplets are reported in Table 2. All of the droplets are prolate spheroids, with the smaller droplets having smaller L values than those of the larger particles. The shape of the largest droplet, Al_{1000}, is relatively independent of temperature, where $L = 0.95$ for $T = 1000$ K and $L = 0.94$ for $T = 1500$, 2000, and 2500 K. The shape of the smallest droplet, Al_{55}, has a stronger dependence on temperature, in particular $L = 0.88$, 0.84, 0.82, and 0.79 for $T = 1000$, 1500, 2000, and 2500 K, respectively. Al_{400} is intermediate between Al_{55} and Al_{1000}, with $L = 0.94$, 0.93, 0.91, and 0.89 for $T = 1000$, 1500, 2000, and 2500 K. We can infer from these results that particles larger than Al_{1000} are essentially spherical, and the shape is almost temperature independent; however, the shapes of smaller particles are prolate and temperature dependent.

4. CONCLUSIONS

In this chapter we summarized the development of analytic potential energy functions for simulating Al nanoparticles. One of the key steps in the development of the analytic potential energy functions was the development of a diverse data set of geometry-dependent atomization energies for Al_2 to Al_{177} that were calculated with validated density functional theory. We have developed two potentials, NP-A[35] and NP-B,[35] that are accurate for clusters, nanoparticles, and bulk crystal properties.

The NP-B[35] analytic potential energy function is an embedded atom model; in particular, it is a reparameterized version of the embedded atom model of Mei and Davenport.[42,43] The original parameterization by Mei and Davenport is less accurate for modeling aluminum clusters and nanoparticles; however, this inaccuracy does not mean that the physical form is not flexible enough to model clusters and nanoparticles. Our results show that the embedded atom functional form of Mei and Davenport is promising when the parameters are adjusted against our cluster and nano-Al data in addition to data for the bulk crystal phases.

The development of the NP-A potential began with an accurate description of diatomic Al. The many-body effects are incorporated through explicit many-body terms. The many-body terms used in the NP-A potential involve screening function and a dependence on coordination number. The physical nature of the screening function is that it weakens the bond between atoms i and j in the presence of other atoms. The coordination number term incorporates the dependence of the bond strength on the coordination numbers of the participating atoms. This bond strength dependence allows for weakening of the bond between atoms i and j as the number of neighboring atoms is increased. We note that the philosophy of NP-A is quite different from that of NP-B. The NP-B analytic potential energy function incorporates the many-body effects through an embedding term, whereas the NP-A potential energy function begins with an accurate description of diatomic Al and uses explicit many-body effects to correct the two-body interaction in the presence of various atomic environments.

We have used the NP-B potential to simulate Al nanodroplets to study the size dependence of densities, thermal expansion, and particle shapes. We have proposed computing the nanoparticle densities by first computing the volumes using overlapping van der Waals spheres. By computing the densities in this way, we obtain densities for the nanodroplets that can be used for comparing the bulk values. We have been able to show that nano-Al droplets have a decreasing coefficient of thermal expansion with decreasing particle size. We have also shown that particle shape is size dependent, with smaller particles being prolate spheroids. The shape of the smallest drop studied, Al_{55}, is more dependent on temperature than is the largest drop, Al_{1000}.

Acknowledgments

We thank Grażyna Staszewska, Przemyslaw Staszewski, and Zhen Hua Li for helpful discussions. This work was supported in part by the Defense-University

Initiative in Nanotechnology (DURINT) of the U.S. Army Research Laborat and the U.S. Army Research Office under agreement DAAD190110503 and the National Science Foundation under grant ITR-0428774.

REFERENCES

1. Armstrong, R. W.; Baschung, B.; Booth, D. W.; Samirant, M. *Nano Lett.*, 200: 253.
2. Rai, A.; Lee, D.; Park, K.; Zachariah, M. R. *J. Phys. Chem. B*, 2004, 108: 1479
3. Meda, L.; Marra, G.; Galfetti, L.; Inchingalo, S.; Severini, F.; De Luca, L. *Com Sci. Technol.*, 2005, 65: 769.
4. Park, K.; Lee, D.; Rai, A.; Mukherjee, D.; Zachariah, M. R. *J. Phys. Chem. B*, 2(109: 7290.
5. Borel, J.-P. *Surf. Sci.*, 1981, 106: 1.
6. Wales, D. J.; Berry, S. R. *J. Chem. Phys.*, 1990, 92: 4283.
7. Mitev, P.; Papageorgiou, D. G.; Lekka, C. E.; Evangelakis, G. A. *Surf. Sci.*, 2(566–568: 937.
8. Werner, R.*Eur. Phys. J. B*, 2005, 43: 47.
9. Alavi, S.; Thompson, D. L. *J. Phys. Chem. A*, 2005, 110: 1518.
10. Born, M.; Huang, K. *The Dynamical Theory of Crystal Lattices*, Oxford Univer Press, London, 1954.
11. Zhan, C.-G.; Zheng, F.; Dixon, D. A. *J. Am. Chem. Soc.*, 2002, 124: 14795.
12. Chaben, G.; Gordon, M. S.; Yarkony, D. R. *J. Phys. Chem. A*, 1997, 101: 7953.
13. Frisch, M. J.; Trucks, G. W.; Schlegel, H. B.; Scuseria, G. E.; Robb, M. A.; Che man, J. R.; Montgomery, J.; et al. *Gaussian 03*, Gaussian, Inc., Pittsburgh, PA, 2(
14. Shim, J.-H.; Lee, B.-J.; Cho, Y. W. *Surf. Sci.*, 2002, 512: 262.
15. Delogu, F. *Phys. Rev. B*, 2005, 72: 205418.
16. Gaudoin, R.; Foulkes, W. M. C. *Phys. Rev. B*, 2002, 66: 52104.
17. Hehre, W. J.; Radom, L.; Schleyer, P. v. R.; Pople, J. A. *Ab Initio Molecular Orb Theory*, Wiley, New York, 1986.
18. Pople, J. A.*Rev. Mod. Phys.*, 1999, 71: 1267.
19. Kohn, W. *Rev. Mod. Phys.*, 1998, 71: 1253.
20. Kohn, W.; Becke, A. D.; Parr, R. G. *J. Phys. Chem.*, 1996, 100: 12974.
21. Lynch, B. J.; Truhlar, D. G. *J. Phys. Chem. A*, 2003, 107: 3898.
22. Schultz, N. E.; Staszewska, G.; Staszewski, P. *J. Phys. Chem. B*, 2004, 108: 485
23. Perdew, J. P.; Burke, K.; Ernzerhof, M. *Phys. Rev. Lett.*, 1996, 77: 3865.
24. Adamo, C.; Cossi, M.; Barone, V. *Theochem*, 1999, 493: 145.
25. Fast, P. L.; Sánchez, M. L.; Truhlar, D. G. *Chem. Phys. Lett.*, 1999, 306: 407.
26. Curtiss, L. A.; Redfern, P. C.; Raghavachari, K.; Rassolov, V.; Pople, J. A. *J. Ch Phys.*, 1999, 110: 4703.
27. McLean, A. D.; Chandler, G. S. *J. Chem. Phys.*, 1980, 72: 5639.
28. Gordon, M. S.; Binkley, J. S.; Pople, J. A.; Pietro, W. J.; Hehre, W. J. *J. Am. Ch Soc.*, 1982, 104: 2797.

29. Francl, M. M.; Pietro, W. J.; Hehre, W. J.; Gordon, M. S.; DeFrees, D. J.; Pople, J. A. *J. Chem. Phys.*, 1982, 77: 3654.
30. Spitznagel, G. W.; Clark, T.; Schleyer, P. v. R. *J. Comput. Chem.*, 1987, 8: 1109.
31. Frisch, M. J.; Pople, J. A.; Binkley, J. S. *J. Chem. Phys.*, 1984, 80: 3265.
32. Krauss, M.; Stevens, W. J. *Annu. Rev. Phys. Chem.*, 1984, 35: 357.
33. Schultz, N. E.; Truhlar, D. G. *J. Chem. Theory Comput.*, 2005, 1: 41.
34. Jaffe, J. E.; Kurtz, R. J.; Gutowski, M. *Comput. Mater. Sci.*, 2000, 18: 199.
35. Jasper, A. W.; Schultz, N. E.; Truhlar, D. G. *J. Phys. Chem. B*, 2005, 109: 3915.
36. Jasper, A. W.; Staszewski, P.; Staszewska, G.; Schultz, N. E.; Truhlar, D. G. *J. Phys. Chem. B*, 2004, 108: 8996.
37. Zope, R. R.; Mishin, Y. *Phys. Rev. B*, 2003, 68: 24102.
38. Daw, M. S.; Baskes, M. I. *Phys. Rev. B*, 1984, 29: 6443.
39. Sutton, A. P.; Chen, J. *Philos. Mag. Lett.*, 1990, 61: 139.
40. Gollisch, H. *Surf. Sci.*, 1986, 166: 87.
41. Ercolessi, F.; Adams, J. *Europhys. Lett.*, 1993: 26.
42. Mei, J.; Davenport, J. W. *Phys. Rev. B*, 1992, 46: 21.
43. Mei, D.; Davenport, J. W.; Fernando, G. W. *Phys. Rev. B*, 1991, 43: 4653.
44. Streitz, F. H.; Mintmire, J. W. *Phys. Rev. B*, 1994, 50: 11996.
45. Joswig, J. O.; Springborg, M. *Phys. Rev. B*, 2003, 68: 85408.
46. Chui, Y. H.; Chan, K. Y. *Phys. Chem. Chem. Phys.*, 2003, 13: 2869.
47. Rodríguez-López, J. L.; Montejano-Carrizales, J. M.; Pal, U.; Sánchez-Ramirez, J. F.; Troiani, H. E.; García, D.; Miki-Yoshida, M.; José-Yacaman, M. *Phys. Rev. Lett.*, 2004, 92: 196102.
48. Campbell, T. J.; Aral, G.; Ogata, S.; Kalia, R. K.; Nakano, A.; Vashishta, P. *Phys. Rev. B*, 2005, 71: 205413.
49. Vashishta, P.; Kalia, R. K.; Nakano, A. *J. Nano. Res.*, 2003, 5: 119.
50. Sun, D. Y.; Gong, X. G. *Phys. Rev. B*, 1998, 57: 4730.
51. Pathak, S.; Shenoy, V. B. *Phys. Rev. B*, 2005, 72: 113404.
52. Rydberg, R. *Z. Phys.*, 1931, 73: 376.
53. Murrell, J. N.; Carter, S.; Farantos, S. C.; Huxley, P.; Varandas, A. J. C. *Molecular Potential Energy Functions,* Wiley, New York, 1984.
54. Stillinger, F. H.; Weber, T. A. *Phys. Rev. B*, 1985, 31: 5262.
55. Ceperley, D. M.; Alder, B. J. *Phys. Rev. Lett.*, 1980, 45: 566.
56. Perdew, J. P.; Zunger, A. *Phys. Rev. B*, 1981, 23: 5048.
57. Schultz, N. E.; Zhao, Y.; Truhlar, D. G. *J. Phys. Chem. A*, 2005, 109: 4388.
58. Pettersson, L. G. M.; Bauschlicher, C. W.; Halicioglu, T. *J. Chem. Phys.*, 1987, 87: 2205.
59. Geske, G.; Boldyrev, A. I. *J. Chem. Phys.*, 2000, 113: 5130.
60. Zope, R. R.; Baruah, T. *Phys. Rev. A*, 2001, 64: 53202.
61. Metropolis, N.; Rosenbluth, A. W.; Rosenbluth, M. N.; Teller, A. H.; Teller, E. *J. Chem. Phys.*, 1953, 21: 1087.
62. Xiang, Y.; Cheng, L.; Cai, W.; Shao, X. *J. Phys. Chem. A*, 2004, 108: 9516.

63. Wales, D. J.; Doye, J. P. K.; Dullweber, A.; Hodges, M. P.; Naumkin, F. Y.; Calv
F.; Hernández-Rojas, J.; Middleton, T. F. *The Cambridge Cluster Database*, http:
www-wales.ch.cam.ac.uk/CCD.html.
64. Silla, E.; Tuñón, I.; Pascual-Ahuir, J. L. *J. Comput. Chem.*, 1991, 12: 1077.
65. Čížek, J. *Adv. Chem. Phys.*, 1969, 14: 35.
66. Purvis, G. D.; Bartlett, R. J. *J. Chem. Phys.*, 1982, 76: 1910.
67. Raghavachari, K.; Trucks, G. W.; Pople, J. A.; Head-Gordon, M. *Chem. Phys. Let*
1996, 157: 479.
68. Woon, D. E.; Dunning, T. H. J. *J. Chem. Phys.*, 1993, 98: 1358.
69. Sarou-Kanian, V.; Millot, F.; Rifflet, J. C. *Int. J. Thermo.*, 2003, 24: 277.
70. Connolly, M. L. *J. Am. Chem. Soc.*, 1985, 107: 1118.